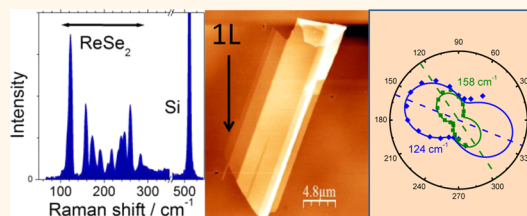# Raman Spectra of Monolayer, Few-Layer, and Bulk ReSe₂: An Anisotropic Layered Semiconductor

Daniel Wolverson,* Simon Crampin, Asieh S. Kazemi, Adelina Ilie, and Simon J. Bending

Department of Physics, University of Bath, Bath BA2 7AY, U.K.

ABSTRACT Rhenium diselenide (ReSe₂) is a layered indirect gap semiconductor for which micromechanical cleavage can produce monolayers consisting of a plane of rhenium atoms with selenium atoms above and below. ReSe₂ is unusual among the transition-metal dichalcogenides in having a low symmetry; it is triclinic, with four formula units per unit cell, and has the bulk space group $P\bar{1}$. Experimental studies of Raman scattering in monolayer, few-layer, and bulk ReSe₂ show a rich spectrum consisting of up to 16 of the 18 expected lines with good

signal strength, pronounced in-plane anisotropy of the intensities, and no evidence of degradation of the sample during typical measurements. No changes in the frequencies of the Raman bands with layer thickness down to one monolayer are observed, but significant changes in relative intensity of the bands allow the determination of crystal orientation and of monolayer regions. Supporting theory includes calculations of the electronic band structure and Brillouin zone center phonon modes of bulk and monolayer ReSe₂ as well as the Raman tensors determining the scattering intensity of each mode. It is found that, as for other transition-metal dichalcogenides, Raman scattering provides a powerful diagnostic tool for studying layer thickness and also layer orientation in few-layer ReSe₂.

KEYWORDS: rhenium diselenide · ReSe₂ · ReS₂ · MoS₂ · monolayer · transition-metal dichalcogenide · band structure · phonon · Raman spectroscopy

One of the least well-known members of the layered transition-metal dichalcogenide (TMD) family[1,2] is the layered semiconductor rhenium diselenide (ReSe₂). We present here a study of its Raman spectra and electronic band structure in monolayer, few-layer, and bulk forms to highlight ways in which ReSe₂ may extend the potential of the TMD materials and provide a means of identifying monolayer and few-layer samples. ReSe₂ is by no means a typical TMD: in brief, its distinctive properties are that (i) it contains some of the heaviest elements of any TMD (so it will show a significant spin−orbit interaction); (ii) it has a large unit cell with no symmetry except a center of inversion; (iii) it has a highly anisotropic structure within the monolayer unit; (iv) it contains metal−metal as well as metal-chalcogen bonds; and (v) its surface is corrugated on the lateral length scale of its unit cell.

The TMDs offer the fascinating possibility of producing relatively large area semiconductors of single molecular layer thickness which may be fabricated into nanoscale device structures utilizing their optical, electronic or spin properties. The TMD family has about 40 members,[1] with single- and few-layer TMD structures and heterostructures having been extensively studied.[2,3] One of the striking properties of TMDs is a transition from an indirect to a direct bandgap semiconductor that often occurs as the thickness is reduced to monolayer (e.g., for MoS₂),[4,5] and we shall show that significant changes in band gap are predicted also for ReSe₂. Furthermore, it has been shown that MoS₂ layers can display high electron mobilities and possess a relatively large spin−orbit interaction compared to graphene,[6,7] opening up new prospects for electronic and spintronic devices[7,8] with work already focusing on scale-up to large area arrays.[9] Besides MoS₂, isoelectronic materials such as WS₂ and WSe₂ are also attracting much attention,[6,10] and these show even larger spin−orbit interactions (about two to three times those of MoS₂[11]). ReSe₂ extends this

family, with one report already of nanosheet transistors based on $ReSe_2$.[12]

In common with other TMDs, bulk $ReSe_2$ is a layered semiconductor in which layers consist of a plane containing metal atoms sandwiched between chalcogen atoms above and below, with layers held together by van der Waals attraction;[1] the perpendicular distance between adjacent Re planes is 6.56 Å, and this is a measure of the thickness of one monolayer (1L). Generally, in the layered TMDs, the two planes of (normally) close-packed chalcogen atoms can stack directly above one another, creating a trigonal metal site, or they can be offset to create an octahedral metal site.[13] However, $ReSe_2$ follows neither of these patterns but crystallizes in the triclinic system, with four formula units per unit cell (see Figure 1a) and the bulk space group $P\bar{1}$. The structure has been determined by X-ray diffraction and consists of one-dimensional chains or ribbons of rhenium atoms arranged in linked Re_4 "lozenge" or "diamond" shapes in the plane,[14−17] with Re in the +4 charge state, as shown in Figure 1(d). This arrangement can be considered as a distortion of the metal ions away from their ideal octahedral sites and the driving force for this distortion (which occurs also in the closely similar ReS_2[18]) has been discussed in terms of Peierls or Jahn−Teller distortions.[13,18,19] Surprisingly, the metal−metal distances in the resulting Re_4 units are comparable to or smaller than those in bulk rhenium metal.[1] The underlying one-dimensional arrangement of rhenium in $ReSe_2$ leads to highly anisotropic properties in the layer plane, as revealed by studies of optical transmission and reflection normal to the layer plane[20−25] and by electron transport in bulk materials.[26] Along with this symmetry breaking by the metal atoms, and again in contrast to MoS_2, the chalcogen atoms are not all equally displaced above and below the Re plane[14] (see Figure 1b,c), resulting in a corrugation of the surface with a vertical amplitude of 0.34 Å.[27] These effects are of interest because the one- or two-dimensional periodicities $ReSe_2$ could impose on other two-dimensional materials if used as a component of multilayer heterostructures.

To investigate monolayer $ReSe_2$ and to provide characterization tools for future work, we have recorded Raman spectra of bulk, few-layer, and monolayer $ReSe_2$ (there are no published Raman spectra of pure $ReSe_2$ in any form though Raman spectra of ReS_2 have been reported[18,28] and there is one report of the Raman scattering of Mo-doped $ReSe_2$).[29] Raman spectroscopy has proven to be invaluable in the characterization of graphene and related 2D materials[30−32] where it can give insight into, for example, layer number[33] and strain.[34] We find Raman spectroscopy can be used to identify monolayer regions but to do so requires a different strategy compared to the case of MoS_2 because the necessary information is contained only in the relative peak intensities and not in Raman
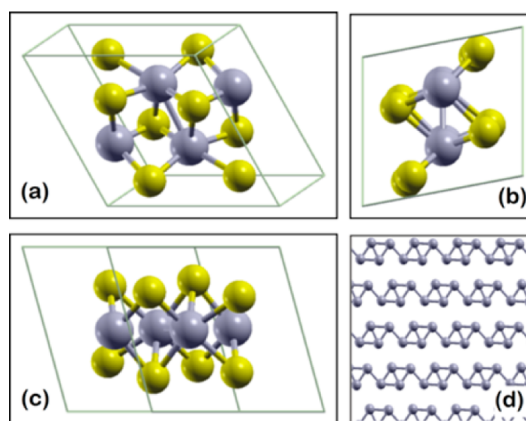

Figure 1. Crystal structure of $ReSe_2$; the rhombohedral unit cell of bulk $ReSe_2$ (yellow, Se; gray, Re) oriented to the (a) ab, (b) bc, and (c) ca planes. (c) Different displacements of the Se atoms normal to the layer plane. (d) In-plane arrangement of the Re atoms (viewed normal to the layer plane), showing the Re chains.

shifts. We further show that Raman spectroscopy can be used to determine the crystallographic orientation of few-layer flakes and that the in-plane anisotropy persists in monolayers, giving optoelectronic properties that will be sensitive to the optical polarization state. We compare our Raman results to first-principles density functional theory (DFT) calculations of the zone-center phonon frequencies for two- and three-dimensional structures. As a necessary part of this DFT work, we also obtain the calculated electronic band structures of bulk and single-layer $ReSe_2$, showing the close-lying direct and indirect band gaps and how these respond to a reduction in dimensionality.

RESULTS AND DISCUSSION

We consider first the electronic band structure of $ReSe_2$. Bulk $ReSe_2$ has been reported experimentally to have an indirect bandgap of 1.18−1.19 eV[20,24,35] and an estimated lowest direct gap at 80 K of 1.401 eV.[21] More precisely, optical absorption studies showed an in-plane anisotropy with room-temperature indirect gaps of 1.17 ± 0.02 and 1.20 ± 0.02 eV for electric fields parallel and perpendicular, respectively, to the direction of the Re chains.[36] In the absorption spectra of thin samples, Jian et al.[35] found clear evidence of excitonic direct band gaps in the range 1.32−1.46 eV. Various calculations of the electronic band structure have been carried out, including using tight-binding,[13] local spherical wave,[19] and full-potential linearized-augmented-plane-wave (FLAPW)[24] methods. In some cases, calculations were carried out only on single layers on the assumption that no significant difference would result in bulk, an assumption which indeed appears to hold for ReS_2.[18]

We have carried out first-principles plane wave density functional theory (DFT) calculations of the band structures of bulk and single-layer structures

and have compared results using norm-conserving and ultrasoft[37] pseudopotentials (NCPP, USPP) and the projector augmented wave[38] (PAW) method. For consistency, most of the results that we shall show were obtained with the PAW approach. For bulk ReSe₂, we took the atomic positions of Lamfers et al.[14] as a starting point and relaxed the structures by total-energy and atomic force minimization. The resulting changes in atomic positions are minimal, even for the case of the out-of-plane displacement of the Se atoms in a monolayer (for which layer separations in the 3D supercell of up to 15 Å were used). In all cases, lattice parameters within 1.3% and cell angles within 0.2% of the experimental values were obtained, with the two-dimensional in-plane lattice parameters changing by less than 0.2% compared to their bulk values evaluated using the same pseudopotentials ($a^{2D} = 6.535$ Å and $a^{3D} = 6.542$ Å for NCPP and 6.669 Å, 6.683 Å, respectively, for PAW; experimental value $a^{3D} = 6.597$ Å[14]). The resulting band structures for bulk and single layer are shown in Figure 2 (top and bottom, respectively); a key to our labeling of special points in the 3D and 2D first Brillouin zones is given in Figure 9 in the Supporting Information.

The band structures presented in Figure 2 show the rather flat nature of the conduction band edge, which leads to several indirect band gaps having very similar energies. We find that the bulk material, Figure 2a, has an indirect gap of 0.98 to 1.06 eV (from USPP and PAW, respectively) with predicted direct gaps of 1.09 eV (at the Brillouin zone boundary along the c^* axis) and 1.31 eV at the Γ point (PAW results). For the monolayer, Figure 2b, we find a significant opening of the gap to 1.34 eV, with the conduction band minimum at the Γ point and the valence band maximum located close to Γ but within the Brillouin zone; we find that this gap remains indirect. In Figure 10 of the Supporting Information we show a calculation of the monolayer band-structure based on a hypothetical monoclinic super-cell; this choice reproduces the above observations but makes the interpretation of the in-plane wavevectors simpler. As pointed out for the similar material ReS₂,[18] an accurate determination of band edge structure requires spin−orbit effects to be taken into account for such heavy atomic species; this is more computa-tionally expensive and is beyond the scope of the present work, but we note that our results above are already in reasonable agreement with experiment and justify the application of first-principles methods also to the phonon modes of ReSe₂.

Measured Raman spectra of ReSe₂ are shown in Figure 3 for layers of thickness 10L and 5L produced by micromechanical cleavage (Figure 3a,b) and a thick flake (Figure 3c). The layer thicknesses are assigned by analysis of the atomic force microscope (AFM) image shown in Figure 3. In the Methods, we outline the steps taken to ensure the reliability of this AFM data
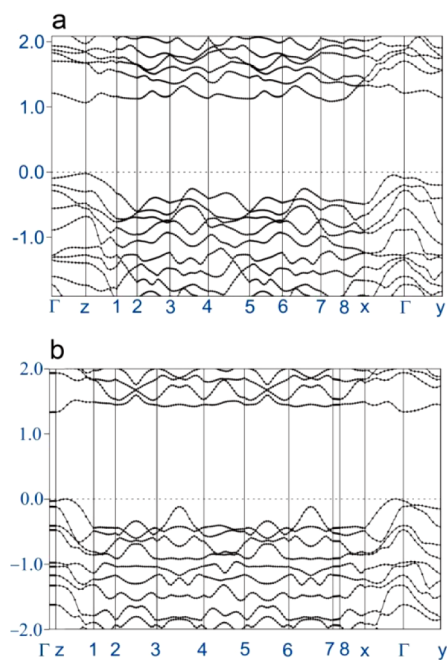

Figure 2. First-principles scalar relativistic projector aug-mented wave calculations of electronic band structures for (a) bulk and (b) single-layer ReSe₂. Vertical axes: energy in eV, taking the highest energy occupied state as the zero of energy (dashed horizontal line). This state does not corre-spond to any special symmetry point in the Brillouin zone. A guide to the labeling of the *k*-points in the 3D and quasi-2D cases is given in Figure 9 of the Supporting Information.

(it is well-known that surface contaminants and inter-calated water can give misleading results). Detailed Raman peak positions and a comparison with our theoretical values obtained using density functional perturbation theory (DFPT) are given in the Supporting Information (Table 1). In Figure 3b, some of the peaks that will be discussed below are highlighted; the peak and shoulder near 124 cm⁻¹ indicated in Figure 3b are in fact a set of four overlapping bands of which two or three are sometimes resolved, depending on crystal orientation as we shall show below. These spectra are qualitatively very similar to that reported for the closely related material ReSe₂:Mo,[29] though that work does not analyze the spectrum in detail. No signals due to ReSe₂ or Re oxides were observed at any higher Raman shifts than those shown, and these spectra can be obtained reproducibly from the same few-layer flakes over several months. Some spectra were recorded at high excitation powers to check for photochemical or thermal degradation or oxidation of the sample, which are expected to result in Raman signals arising from metal oxides[39,40] such as Re₂O₇,[41] ReO₃,[42] or elemental chalcogens known to precipitate out from many chal-cogenides under photoexcitation.[43] No such signals were observed even up to powers sufficient to punc-ture a thick ReSe₂ layer. This robustness to oxidation suggests that laser-thinning of ReSe₂ to manufacture controlled single-layer regions from thick layers will be possible, as recently demonstrated for MoS₂.[44]
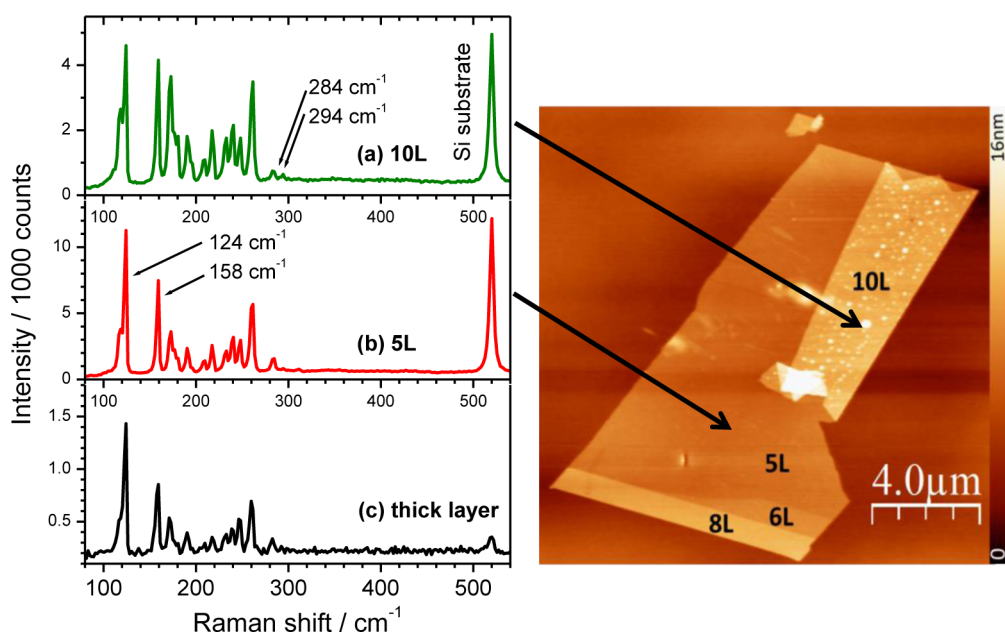
Figure 3. Raman scattering spectra of ReSe$_2$ on a SiO$_2$/Si substrate for (a) 10 layers; (b) 5 layers, and (c) a thick flake. A contact-mode AFM image of the sample from which spectra (a) and (b) were obtained is shown on the right, with the thickness of various layers labeled. The peaks between 100 and 300 cm^{-1} are all due to triclinic ReSe$_2$, and the peak at 521 cm^{-1} is due to the (001)-oriented silicon substrate, which is observed due to transmission through the sample. The spectra are un-normalized to indicate typical relative intensities under similar experimental conditions.

In agreement with our DFPT predictions, the ReSe$_2$ Raman modes occupy the frequency range from 100 to 300 cm^{-1} and are densely spaced, with the exception of a gap around 140 cm^{-1} (see the Supporting Information, Table 1 and Figure 11). Note that we are considering here only Brillouin zone-center phonons, which participate in first-order Raman scattering. As ReSe$_2$ has 12 atoms per unit cell, we expect 36 normal modes. Given the unit cell point group symmetry C_i, with only identity and inversion symmetry elements, and since all atoms are displaced from the inversion center[14] (see Figure 1), all normal modes are nondegenerate; there are 18 Raman-active A_g modes, 15 infrared active A_u modes, and 3 zero-frequency A_u modes. Experimentally, we find that up to 16 modes are required to fit the spectra, of which the highest-frequency A_g mode (experimental Raman shift 294 cm^{-1}) is found to be very weak and is sometimes not observed. Most of the remaining peaks are predicted to overlap substantially, accounting for the difficulty of fitting the spectra to locate all 18 Raman-active modes.

Figure 4 maps the un-normalized intensity distribution of selected Raman modes over the ReSe$_2$ flakes and supporting Si substrate whose spectra have been presented in Figure 3. The colors of the upper flake in Figure 4a indicate that the 5L and 10L regions are sufficiently transparent at visible wavelengths to display interference effects, whereas the thick flake is highly reflective and appears yellow-white. This is confirmed by the strength of the Si Raman mode, Figure 4c), which can be observed in transmission
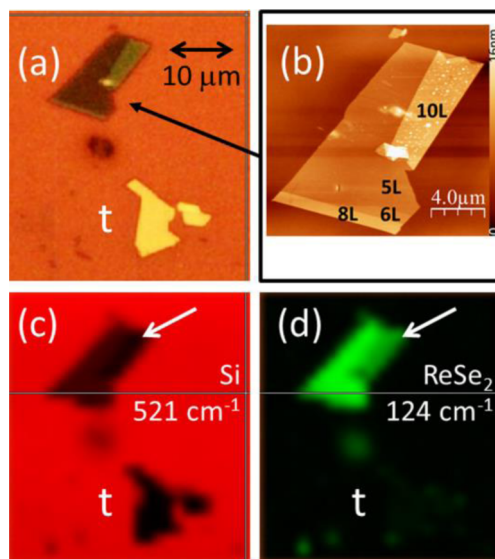

Figure 4. (a) Optical micrograph of the ReSe$_2$ flakes whose Raman spectra are shown in Figure 3. (b) Contact mode AFM image of the thinner flake, repeated from Figure 3 for convenience. (c) Spatial intensity distribution of the 521 cm^{-1} mode of the Si substrate. (d) Spatial intensity distribution of the 124 cm^{-1} band of ReSe$_2$ (increasing false color brightness indicates increasing Raman signal). The thick, highly reflective flake is labeled t; its signals are relatively weak and so it is not visible in (d). The white arrow indicates the 10L region in (c) and (d).

through the ReSe$_2$, being strongest for the 5L region, weaker for the 10L region indicated by the white arrow, and weakest of all for the thick flake. Figure 4d and Figure 3a−c show that the Raman signals of the ReSe$_2$ do not scale proportionally with thickness, which is
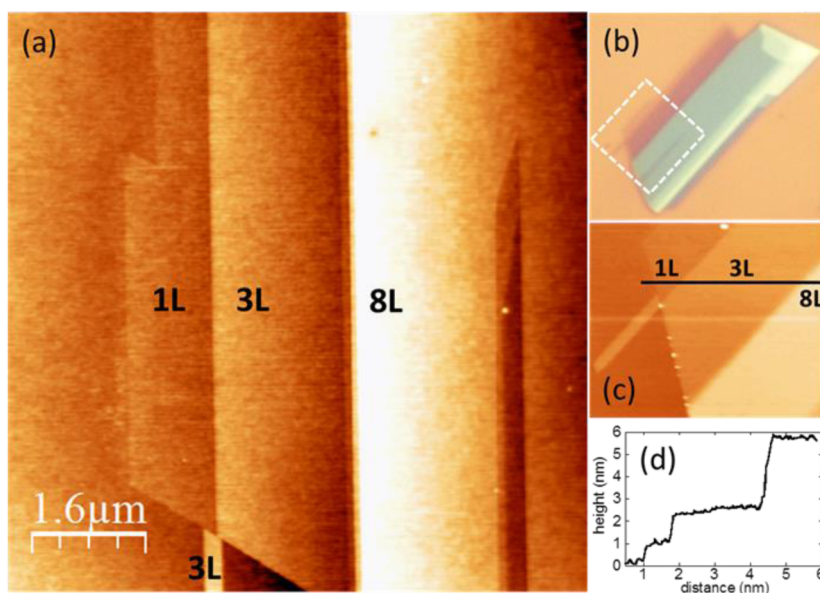
Figure 5. (a) Contact mode AFM image of part of the second sample, showing regions of thickness 1L, 3L, and 8L. (b) Optical image of the whole of this sample under illumination conditions which maximize the color contrast between different layer thicknesses; the dashed white box identifies the region imaged by AFM in (a). (c) Contact mode AFM image of the lower end of the sample. The black line shows the position of the topographic line scan giving the height profile shown in (d).

due to interference effects since the flakes are supported on a conventional SiO_2/Si substrate. We analyze this effect quantitatively in the Supporting Information (Figure 12).

We note that the $ReSe_2$ Raman bands shown in Figure 3 appear with different relative strengths for different layer thicknesses; compare, for instance the 124 and 159 cm^{-1} bands in Figure 3a–c. This implies that the relative intensities of the bands are dependent either on orientation, as expected for this low-symmetry material, or on sample thickness, or both of these. To clarify this, we measured polarization-dependent Raman spectra on a second flake containing regions of thickness 1L, 3L, and 8L as shown in Figure 5a–c. A topographic line scan (Figure 5d) indicates a monolayer step height of ∼7 Å, consistent with the crystallographic layer thickness of 6.56 Å, and confirms that this sample contains a monolayer (1L) region. It is clear from the morphology indicated in the images of Figure 5 that the 1L, 3L and 8L regions all have the same orientation, enabling us to separate orientation and thickness effects in the Raman spectra.

For the Raman measurements on this sample, the excitation spot was held at a fixed point on the 8L region and the plane of polarization of the incident light was rotated in the layer plane. No analyzer was used before the detector, and our detection system is polarization-insensitive in this wavelength region (this is demonstrated in the Supporting Information, Figure 13). Thus, we do not expect to observe any angular dependence of the Raman signal for the (001)-oriented Si substrate since outgoing polarizations parallel and perpendicular to the excitation polarization are detected with equal sensitivity and, given the form

of the Raman tensor of cubic silicon, their summed intensity is a constant.[45] This is confirmed by the experimental results for the Si Raman mode presented in the right-hand section of Figure 6.

Conversely, the Raman peaks of $ReSe_2$ show a clear variation of intensity with the angle of rotation of the excitation polarization for all modes. The observed angle dependences can therefore be attributed to the structure of the Raman tensors for each mode. To analyze this behavior in detail we focus on the group of overlapping bands from 110 to 124 cm^{-1} and the peak at 158 cm^{-1} which exhibit a good signal-to-noise at all orientations. As shown in Figure 6, these two bands have their maximum intensities at different orientations, indicating significant differences in their Raman tensors. The 124 and 158 cm^{-1} modes are advantageous in not having neighboring peaks to at least one side since they bracket the "gap" in the Raman spectrum around 140 cm^{-1}; this makes fitting more reliable. We note that calculated atomic displacements for the Γ-point modes of $ReSe_2$ indicate that the vibrational modes cannot be classified simply as either in-plane or out-of-plane oscillations, but those below the "gap" mainly involve twisting and rocking motions in which the Re atoms undergo significant displacements, whereas higher-frequency modes involve stretching and wagging motions of the lighter Se atoms.

We now consider whether the pronounced angle-dependence of the Raman spectra can be used to determine the orientation of a given flake. Clearly, the morphology of cleaved flakes already gives a strong clue, since cleavage edges often lie along the in-plane a and b axes,[46–48] though it is not always possible to distinguish between a and b axes visually,
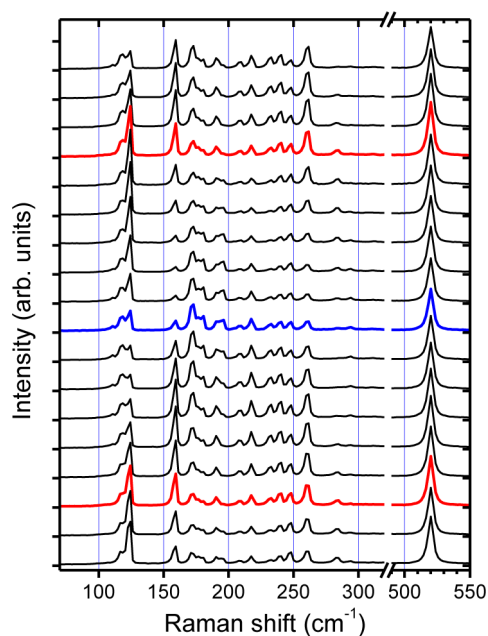
Figure 6. Raman spectra of ReSe$_2$ as a function of the angle of rotation of the excitation polarization; spectra were recorded as the incident polarization was rotated in 15° steps and are offset vertically for clarity. The detection was unpolarized, resulting in a constant intensity for the Si Raman peak at 520 cm^{-1}. The zero of the angle scale is defined by the experimental setup and so is arbitrary with respect to the crystallographic axes of the sample. The spectra are un-normalized. The red (0° and 180°) and blue (90°) spectra are highlighted to demonstrate that the same spectrum is obtained after rotation of the excitation polarization by 180°.

and indeed, micromechanical exfoliation frequently yields very irregular shapes where such edges cannot even be identified. For layers grown by any kind of vapor deposition, morphological information will not be available, and an important task will be to map out the domain structure in the film. We therefore seek to establish whether Raman spectra can provide an *absolute* determination of crystal orientation with respect to the in-plane x axis in the laboratory reference frame, and also whether Raman spectra can highlight *relative* changes in orientation from one crystal to another. In a mapping experiment, collection of an exhaustive set of data such as that of Figure 6 at each pixel is not practical and it is important to know how much information about relative orientation can be gained from just a single spectrum.

To answer this, we consider the Raman tensor R (for a given mode) relevant to light polarized in the layer plane. The incident and scattered polarization vectors are e_i, e_s, respectively, and these may be written as two-dimensional vectors; then, the relevant part of R has the symmetric form

$$R = \begin{pmatrix} u & v \\ v & w \end{pmatrix} \qquad (1)$$

where u, v, and w are constants for that mode which we can obtain either from our DFPT calculations or by

fitting experimental data, as follows. The observed scattering intensity of the chosen mode may be expressed in general as I where $I \propto |e_i R e_s|^2$. Conventionally, one would introduce a linear polarization analyzer into the detection system and could then obtain u, v and w separately for each mode.[49] However, this requires at least three spectra to be recorded, with incident and scattered polarizations (x,x), (y,y), and (x,y), and so is impractical for mapping purposes.

For the particular case of unpolarized detection where the incident polarization makes an angle θ to the crystal a axis, the total recorded intensity $I_T(\theta)$ is the sum of the scattered intensities in the polarization directions parallel and perpendicular to the excitation polarization and is

$$I_T(\theta) \propto u^2 \cos^2\theta + w^2 \sin^2\theta + v^2 + 2v(u+w)\sin\theta\cos\theta \qquad (2)$$

For an arbitrary in-plane orientation of the crystal in the laboratory frame, fitting the above expression to the angular variation of the intensity of the chosen mode only requires three independent parameters u′, v′, and w′, which are the components of the effective Raman tensor R′ (which is R transformed into the laboratory frame by a rotation ϕ about the layer normal). By comparison of the angular dependences of the Raman mode predicted from the first-principles tensor R and the experimental tensor R′, one can therefore measure the absolute rotation ϕ of the crystal with respect to the laboratory axes. The accuracy of this process will be limited ultimately by the accuracy with which one can calculate the components of R by first-principles methods. This is a challenging task and has only recently become possible using widely available DFT codes; the results in Figure 7 illustrate that this can be done successfully. We have used two types of pseudopotential (see the Methods) and find good agreement between the two; a specimen set of Raman tensor components calculated using norm-conserving pseudopotentials is presented in the Supporting Information (Table 2).

In Figure 7a, we show fits of eq 2 to peak intensities recorded experimentally as the excitation polarization is rotated. For the well-resolved 124 cm^{-1} mode and also for the 110 cm^{-1} mode, this expression fits the data well but fails for the unresolved central pair of modes, indicating a superposition of different angular variations. The dashed lines indicate the directions in which the strongest scattering is obtained for each of these two modes (given values of the parameters $u-w$, one can obtain the angles corresponding to this direction analytically, see the Supporting Information, eq 3). Simulations of the expected intensity variation with angle for these modes are shown in Figure 7b and reproduce the experimental observations well. By comparing the dashed lines in (a) and (b), it is easy to see that the two patterns are rotated with respect to
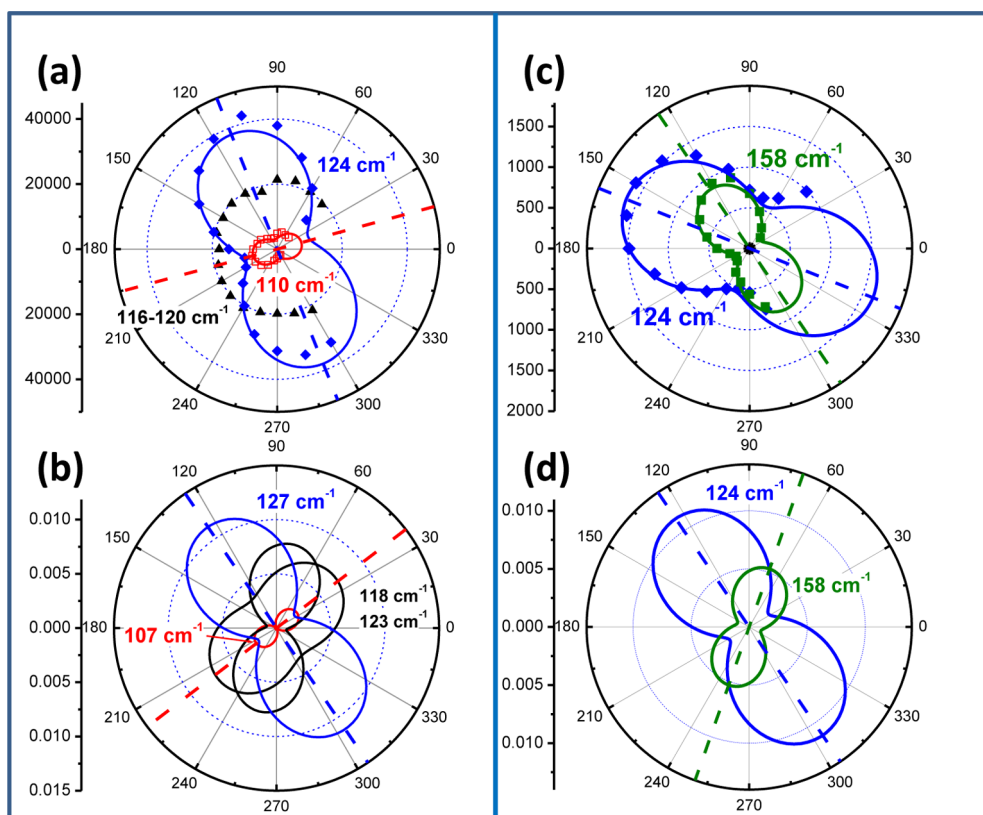
Figure 7. (a) Measured peak intensities of the 124 cm^{-1} (blue diamonds) and 110 cm^{-1} (red squares) modes of ReSe$_2$ as a function of the excitation polarization direction, obtained using the sample shown in Figure 3. The zero angle is defined by the experimental system. Also shown (black triangles) are the peak intensities of the overlapping 116 and 120 cm^{-1} modes. The solid lines are fits of eq 2 to the data for the 124 and 110 cm^{-1} modes with the dashed lines of the same colors showing the angles for which the Raman intensity is maximum. (b) Angular dependence of the peak intensities calculated from eq 2 using tensor components derived from the first-principles DFPT calculations. (c) Measured and (d) calculated angle dependence of the peak intensities using the 124 and 158 cm^{-1} modes (blue circles and green squares respectively) obtained as for (a) and (b) but for the sample of Figures 5 and 6.

one another by the angle ϕ between the in-plane crystal axes and the laboratory axes. From the results of Figure 7, we can determine that the first sample is rotated with respect to the laboratory axes by an angle in the range $-13°$ (using the 124 cm^{-1} mode data) to $-22°$ (from the 110 cm^{-1} mode) or an average rotation of $-17.5°$. Other modes give results consistent with this range. The uncertainties in the experimental angles are of order $\pm2°$ and are dominated by the difficulties in fitting the peak intensities of partially overlapping bands; the remaining discrepancy between the absolute rotations determined from the different modes must be ascribed to the limited accuracy of the calculated Raman tensors. By measurement of the optical micrographs of Figure 4, we find that the lower cleaved edge of the sample is rotated with respect to the laboratory x axis by $-15.6°$, in remarkably good agreement with the figure of $-17.5°$ derived from the first-principles methods. Similarly for the second sample, Figure 7c,d, the angle dependence patterns of the 124 and 158 cm^{-1} modes are displaced from the DFPT predictions by an average of $+44°$, and this corresponds well to the orientation of the long cleaved edge of the sample ($+42°$) as measured from

the image shown in Figure 4b. These results clearly demonstrate that determination of the absolute orientation of ReSe$_2$ samples is possible given knowledge of the calculated Raman tensors.

Determining relative orientation of flakes or domains is an easier problem to address. First, we have checked that this is feasible by the simple expedient of measuring the angle-dependent Raman scattering of a chosen flake, rotating the flake by 90° and measuring its angle dependence again. Results are shown in the Supporting Information (Figure 14) and do indeed confirm that the whole pattern is rotated by 90 $\pm$ 2°. A more challenging test of this idea is provided by the 5L and 10L regions of the first sample discussed above since the Raman spectra of these two regions show different peak height relationships, for example, the 124 and 158 cm^{-1} peaks in Figure 3. The most likely explanation for this is that the 5L and 10L regions have different orientations; indeed, most probably, the 10L region is a piece of the 5L material folded back on itself. Inspection of Figure 4b shows that their long left-hand cleavage edges are misaligned by approximately 10°. By measuring the angle dependence of the Raman scattering from these two regions (shown in the
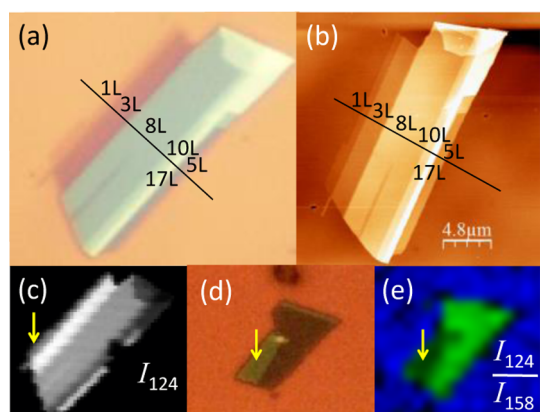
Figure 8. (a) Optical micrograph of the ReSe$_2$ sample whose Raman spectra are shown in Figure 6. (b) Tapping mode AFM image of the same sample identifying the numbers of layers within the flake. (c) Raman map of the intensity of the 124 cm^{-1} band, I_{124} with the position of the 1L region marked by the arrow. (d) Optical micrograph of the flake whose Raman spectra are shown in Figure 5. (e) Raman map of the sample shown in (d), in which the false color scale is derived from the ratio of intensity of the 124 to the 158 cm^{-1} Raman bands. In (d) and (e), the position of the 10L region is marked by an arrow.

Supporting Information, Figure 15) and fitting with eq 2 as above, we find a displacement of $6 \pm 2°$ between the angle dependences of the two regions. Once more, this is in reasonable agreement with the evidence from the sample morphology. The angular variation exhibited by the 10L region is noticeably broader than that of the 5L region, which is expected if the 10L region is folded, as its Raman signals will contain contributions from both the upper, displaced layer and the lower, unaffected layer. The cumulative spectra would broaden the angle dependence and reduce the inferred relative rotation, as observed. It thus appears that careful analysis of the angle-dependent Raman scattering may even be able to reveal mis-orientation of stacked multilayers, again an important capability if layers are grown by vapor deposition.

Finally, we consider what can be learned from a single spectrum, as would be obtained at each pixel in a mapping experiment. First, we consider the Raman spectra of the 1L region in more detail. Parts a and b of Figure 8 show optical and AFM images of the whole of the second sample for comparison with Raman mapping experiments. Illumination conditions were optimized when Figure 8a was recorded in order to enhance the contrast between 1L, 3L, and 8L regions (the images for comparison with the Raman mapping data were collected in a different optical microscope and so the colors are not directly comparable). First, we note that there is no observed (or predicted) shift in the frequencies of any Raman bands from their bulk values, so that no indication of sample thickness can be obtained from peak shifts alone. This is in agreement with the recent observations on ReS$_2$.[18] Although Raman scattering will therefore not be as informative

as it is for MoS$_2$ and graphene, it should be noted that Raman mapping will still be vital in confirming orientation and layer composition (especially if multilayers of different materials are present), so that it is still worth examining whether it can simultaneously provide thickness information. It is known that interference effects between the Si substrate and the SiO$_2$ and TMD layers modulate Raman intensities; this was noted in graphene[50−52] and was recently analyzed in detail for few-layer TMDs.[53] We have applied the analysis of Li et al.[53] to estimate the variation in Raman intensity as a function of layer thickness and Raman shift (Figure 12, Supporting Information).

Since the peak intensities are sensitive to layer thickness as well as orientation, variations in intensity of a *single* peak could arise from changes in either. However, if the ratio of the intensities of *two* different peaks is taken, for example, $r = I_{124}/I_{158}$, which is a straightforward process in most mapping software, then any intensity changes due to variation in thickness will cancel, with the resulting ratio r a function of orientation ϕ alone. We note that a second advantage of using unpolarized detection, apart from speed of measurement, is that peak intensities are unlikely to become vanishingly small for any ϕ, and so r should always remain finite. Unfortunately, the value of r cannot be used to extract the absolute orientation of a region directly, since, from consideration of eq 2, analysis shows that, given u, v, and w values for two modes, r could result from four possible angles ϕ. Nevertheless, a false color scale based on r will yield a valuable, visual confirmation of the extent of single crystal domains in a layer. A given domain can then, if necessary, be fully characterized by an angle-dependent study at a single representative point. We provide an example of this in Figure 8d,e, using the folded flake we have discussed above, where full sets of angle-dependent measurements already confirmed that the thicker region is mis-oriented with respect to the thinner region. Figure 8e shows a false color map of this flake based on $r = I_{124}/I_{158}$, and it is clear that the darker green region corresponds to the misaligned region. Unlike the maps of the same flake shown previously in Figure 4, this new map is based only on crystallographic orientation and the effects of thickness have been eliminated. This approach therefore represents a powerful and practical method for the characterization of ReSe$_2$ and is expected to be applicable to anisotropic few-layer materials in general.

CONCLUSIONS

We have obtained Raman spectra for monolayer, few-layer, and bulk ReSe$_2$ and compared them with the results of first-principles density functional theory calculations. Good agreement exists between the number and frequency positions of measured and calculated vibrational modes. Calculations also reproduce the

magnitude and indirect nature of the semiconductor band gap for bulk material. Furthermore, we show that the relative intensities of the Raman bands are highly sensitive to the orientation of the in-plane crystallographic axes for few-layer samples, enabling polarized Raman spectroscopy to determine the absolute and relative in-plane orientation of samples of arbitrary shape down to a single monolayer in thickness. We provide a practical strategy for obtaining a rapid assessment of the distribution of domain orientations in an inhomogeneous layer. Finally, interference effects in the Raman spectra of $ReSe_2$ on SiO_2 layers on Si substrates have been analyzed. The signals do not allow an unambiguous measurement of the thickness of a particular layer in isolation but vary sufficiently strongly with thickness to give contrast, for example, between monolayer regions and regions of thickness from two to six monolayers, so that single monolayers can be identified by comparison in a mixed, few-layer sample.

MATERIALS AND METHODS

Samples of bulk single crystal $ReSe_2$ and also $ReSe_2$ flakes produced by micromechanical cleavage and transferred onto 90 nm thick SiO_2 on a Si wafer were obtained commercially from 2D Semiconductors, El Cerrito, CA (www.2dsemiconductors.com). The bulk crystals were prepared by vapor transport according to the method of Huang et al.[54] from high-purity initial reagents and crystalline purity is better than 99.995%.

A combination of amplitude-modulated (AM) tapping mode and contact mode AFM was used to determine the thickness of $ReSe_2$ layers within multilayer flakes; for this we utilized an Asylum Research MFP3D microscope, and Olympus AC240TS, and Nanosensors PPP-CONT cantilevers with nominal spring constants of 2 and 0.2 N/m, respectively. It is well-known that the observed step height between two different materials can differ greatly from the real value when tapping mode AFM is used[55] without appropriate precautions. Here we used oscillation conditions and set-points such that the average dynamic force between the tip and surface during an oscillation period has repulsive character on all surfaces involved; this allowed us to minimize artifacts when determining the number of layers at the interface between the $ReSe_2$ flakes and the SiO_2 substrate, in a similar way as for graphene flakes.[56] Moreover, corroboration with contact-mode AFM, where a static repulsive force is produced, led to agreement regarding the assignment of monolayer regions in Figures 5 and 8. Scanning in contact mode AFM used low repulsive forces in order to minimize further errors in the measured layer thickness caused by coupled frictional, lateral forces that can twist the cantilever and affect the measurement of the normal force. We also note that no water layers appear to be intercalated between the $ReSe_2$ flakes and the substrate, since the obtained topographic profiles (e.g., Figure 5d) correspond well to the expected van der Waals spacing.

Raman spectra were recorded using a Renishaw inVia Raman microscope with a ×50 objective lens and lateral spatial resolution of around 1 μm. Incident powers were kept low (~50 to 100 μW) and acquisition times were typically 100 to 300 s. Excitation wavelengths of 532 and 785 nm were used, both allowing the acquisition of good spectra. The presented data were taken using 532 nm excitation. The excitation polarization was determined at the objective lens by reference to a wire grid polarizer and was rotated by means of a half-wave plate inserted in the excitation beam path inside the spectrometer. No polarization analyzer was used in the detection system, which was insensitive to polarization for Raman shifts up to 300 cm^{-1}. Where the intensity of a Raman band is mentioned, we mean by this the peak area obtained by fitting using a purely Lorentzian line shape after subtraction of a smooth background.

First-principles density functional theory (DFT) using a plane-wave basis set was carried out using both norm-conserving (NCPP) and scalar relativistic ultrasoft[37] pseudopotentials in the local density approximation (LDA) and also a scalar relativistic projector augmented wave[38] (PAW) method in the generalized gradient approximation (GGA). Since the PAW pseudopotential for Re has not been widely applied, it and the NCPP for Re were tested on other materials including hexagonal Re metal, for which lattice parameters within +0.8% and −0.8%, respectively, of the experimental value were obtained. Additional testing for $ReSe_2$ through comparison with the outputs of CASTEP[57] (norm-conserving and ultrasoft pseudopotentials) and Quantum ESPRESSO[58] (using norm-conserving pseudopotentials and PAW) DFT codes also gave acceptable agreement. Following systematic convergence testing, results presented were obtained with kinetic energy cutoff (60 Ry for NCPP and PAW); charge density cutoff (300 Ry for PAW); k-point sampling, for both PAW and NCPP: $8 \times 8 \times 8$ (bulk) or $8 \times 8 \times 1$ (monolayer) Monkhorst−Pack grids.[59] Phonon frequencies and Raman scattering intensities were calculated via DFPT[60] in both CASTEP and Quantum ESPRESSO, including tests with k-point sampling increased to $10 \times 10 \times 10$, and were again in good agreement (maximum discrepancy in frequency was of order 3%).

Conflict of Interest: The authors declare no competing financial interest.

Supporting Information Available: Diagrams (plotted using Xcrysden[61]) of the first Brillouin zone for bulk $ReSe_2$ and the effective first Brillouin zone used for the DFT calculations on monolayer $ReSe_2$ (Figure 9), electronic band structure of monolayer $ReSe_2$ calculated with adjacent layers in the supercell displaced along the normal to the layer plane (Figure 10), list of observed and calculated Raman frequencies for bulk $ReSe_2$ (Table 1), scatter plot of the vibrational frequencies measured by Raman spectroscopy and those calculated by DFT/DFPT for single-layer and bulk $ReSe_2$ (Figure 11), experimental data and simulation of the dependence of the Raman scattering intensity on the number of layers of $ReSe_2$ on a 90 nm SiO_2 layer on a Si substrate (Figure 12), demonstration of the polarization insensitivity over 100−300 cm^{-1} of the Raman spectrometer used in this work (Figure 13), calculated Raman tensor components of all the Raman-active modes of $ReSe_2$ (Table 2), equations to obtain the orientation of a layer from the fitted Raman tensor components (eq 3), change in the polarization dependence of the Raman scattering on rotating a $ReSe_2$ flake by 90° with respect to the laboratory axes (Figure 14), and polarization dependence of the Raman scattering from two mis-aligned regions of a single $ReSe_2$ flake (Figure 15). This material is available free of charge via the Internet at http://pubs.acs.org.

REFERENCES AND NOTES

1. Wilson, J. A.; Yoffe, A. D. The Transition Metal Dichalcogenides: Discussion and Interpretation of the Observed Optical, Electrical and Structural Properties. *Adv. Phys.* **1969**, *18*, 193–335.
2. Geim, A. K.; Grigorieva, I. V. Van der Waals Heterostructures. *Nature* **2013**, *499*, 419–425.
3. Wang, Q. H.; Kalantar-Zadeh, K.; Kis, A.; Coleman, J. N.; Strano, M. S. Electronics and Optoelectronics of Two-Dimensional

Transition Metal Dichalcogenides. *Nat. Nanotechnol.* **2012**, *7*, 699–712.

4. Mak, K.; Mak, C.; Lee, J.; Hone, J.; Shan, T.; Heinz Atomically Thin MoS$_2$: A New Direct-Gap Semiconductor. *Phys. Rev. Lett.* **2010**, *105*, 136805.

5. Splendiani, A.; Splendiani, L.; Sun, Y.; Zhang, T.; Li, J.; Kim, C.-Y.; Chim, G.; Galli, F.; Wang Emerging Photoluminescence in Monolayer MoS$_2$. *Nano Lett.* **2010**, *10*, 1271–1275.

6. Feng, W.; Feng, Y.; Yao, W.; Zhu, J.; Zhou, W.; Yao, D.; Xiao Intrinsic Spin Hall Effect in Monolayers of Group-VI Dichalcogenides: A First-Principles Study. *Phys. Rev. B* **2012**, *86*, 165108.

7. Xiao, D.; Xiao, G.-B.; Liu, W.; Feng, X.; Xu, W.; Yao Coupled Spin and Valley Physics in Monolayers of MoS$_2$ and Other Group-VI Dichalcogenides. *Phys. Rev. Lett.* **2012**, *108*, 196802.

8. Radisavljevic, B.; Radisavljevic, A.; Radenovic, J.; Brivio, V.; Giacometti, A.; Kis Single-Layer MoS$_2$ Transistors. *Nat. Nanotechnol.* **2011**, *6*, 147–150.

9. Nam, H.; Nam, S.; Wi, H.; Rokni, M.; Chen, G.; Priessnitz, W.; Lu, X.; Liang Mos$_2$ Transistors Fabricated *Via* Plasma-Assisted Nanoprinting of Few-Layer MoS$_2$ Flakes into Large-Area Arrays. *ACS Nano* **2013**, *7*, 5870–5881.

10. Zhao, W.; Zhao, Z.; Ghorannevis, L.; Chu, M.; Toh, C.; Kloc, P.-H.; Tan, G.; Eda Evolution of Electronic Structure in Atomically Thin Sheets of WS$_2$ and WSe$_2$. *ACS Nano* **2013**, *7*, 791–797.

11. Zhu, Z. Y.; Cheng, Y. C.; Schwingenschlögl, U. Giant Spin-Orbit-Induced Spin Splitting in Two-Dimensional Transition-Metal Dichalcogenide Semiconductors. *Phys. Rev. B* **2011**, *84*, 153402.

12. Yang, S. X.; Tongay, S.; Li, Y.; Yue, Q.; Xia, J. B.; Li, S. S.; Li, J. B.; Wei, S. H. Layer-Dependent Electrical and Optoelectronic Responses of ReSe$_2$ Nanosheet Transistors. *Nanoscale* **2014**, *6*, 7226–7231.

13. Kertesz, M.; Kertesz, R.; Hoffmann Octahedral *vs.* Trigonal-Prismatic Coordination and Clustering in Transition-Metal Dichalcogenides. *J. Am. Chem. Soc.* **1984**, *106*, 3453–3460.

14. Lamfers, H. J.; Meetsma, A.; Wiegers, G. A.; deBoer, J. L. The Crystal Structure of Some Rhenium and Technetium Dichalcogenides. *J. Alloys Compd.* **1996**, *241*, 34–39.

15. Wildervanck, J. C.; Wildervanck, F.; Jellinek The Dichalcogenides of Technetium and Rhenium. *J. Less-Common Met.* **1971**, *24*, 73–81.

16. Alcock, N. W.; Kjekshus, A. Crystal Structure of ReSe$_2$. *Acta Chem. Scand.* **1965**, *19*, 79.

17. Seley, D. B.; Nath, M.; Parkinson, B. A. ReSe$_2$ Nanotubes Synthesized from Sacrificial Templates. *J. Mater. Chem.* **2009**, *19*, 1532–1534.

18. Tongay, S.; Sahin, H.; Ko, C.; Luce, A.; Fan, W.; Liu, K.; Zhou, J.; Huang, Y.-S.; Ho, C.-H.; Yan, J.; *et al.* Monolayer Behaviour in Bulk ReS$_2$ Due to Electronic and Vibrational Decoupling. *Nat. Commun.* **2014**, *5*, 3252.

19. Fang, C. M.; Wiegers, G. A.; Haas, C.; deGroot, R. A. Electronic Structures of Res$_2$, ReSe$_2$ and TcS$_2$ in the Real and the Hypothetical Undistorted Structures. *J. Phys.: Condens. Matter* **1997**, *9*, 4411–4424.

20. Marzik, J. V.; Kershaw, R.; Dwight, K.; Wold, A. Photoelectronic Properties of ReS$_2$ and ReSe$_2$ Single Crystals. *J. Solid State Chem.* **1984**, *51*, 170–175.

21. Ho, C. H.; Liao, P. C.; Huang, Y. S.; Tiong, K. K. Temperature Dependence of Energies and Broadening Parameters of the Band-Edge Excitons of ReS$_2$ and ReSe$_2$. *Phys. Rev. B* **1997**, *55*, 15608–15613.

22. Ho, C. H.; Liao, P. C.; Huang, Y. S.; Yang, T. R.; Tiong, K. K. Optical Absorption of ReS$_2$ and ReSe$_2$ Single Crystals. *J. Appl. Phys.* **1997**, *81*, 6380–6383.

23. Ho, C. H.; Huang, Y. S.; Tiong, K. K.; Liao, P. C. Absorption-Edge Anisotropy in ReS$_2$ and ReSe$_2$ Layered Semiconductors. *Phys. Rev. B* **1998**, *58*, 16130–16135.

24. Ho, C. H.; Huang, Y. S.; Chen, J. L.; Dann, T. E.; Tiong, K. K. Electronic Structure of ReS$_2$ and ReSe$_2$ from First-Principles Calculations, Photoelectron Spectroscopy, and Electrolyte Electroreflectance. *Phys. Rev. B* **1999**, *60*, 15766–15771.

25. Ho, C. H.; Huang, Y. S.; Liao, P. C.; Tiong, K. K. Crystal Structure and Band-Edge Transitions of ReS$_{2-x}$Se$_x$ Layered Compounds. *J. Phys. Chem. Solids* **1999**, *60*, 1797–1804.

26. Ho, C. H.; Huang, Y. S.; Tiong, K. K. In-Plane Anisotropy of the Optical and Electrical Properties of ReS$_2$ and ReSe$_2$ Layered Crystals. *J. Alloys Compd.* **2001**, *317*, 222–226.

27. Parkinson, B. A.; Ren, J.; Whangbo, M. H. Relationship of STM and AFM Images to the Local Density of States in the Valence and Conduction Bands of Rhenium Selenide (ReSe$_2$). *J. Am. Chem. Soc.* **1991**, *113*, 7833–7837.

28. Downs, R. T. In *The Ruⵉ Project: An Integrated Study of the Chemistry, Crystallography, Raman and Infrared Spectroscopy of Minerals*, 19th General Meeting of the International Mineralogical Association, Kobe, Japan, 2006; O03−13.

29. Yang, S. X.; Tongay, S.; Yue, Q.; Li, Y. T.; Li, B.; Lu, F. Y. High-Performance Few-Layer Mo-Doped ReSe$_2$ Nanosheet Photodetectors. *Sci. Rep.* **2014**, *4*, 6.

30. Calizo, I.; Calizo, S.; Ghosh, W.; Bao, F.; Miao, C.; Ning Lau, A.; Balandin, Raman Nanometrology of Graphene: Temperature and Substrate Effects. *Solid State Commun.* **2009**, *149*, 1132–1135.

31. Graf, D.; Molitor, F.; Ensslin, K.; Stampfer, C.; Jungen, A.; Hierold, C.; Wirtz, L. Spatially Resolved Raman Spectroscopy of Single- and Few-Layer Graphene. *Nano Lett.* **2007**, *7*, 238–242.

32. Mohiuddin, T.; Mohiuddin, A.; Lombardo, R.; Nair, A.; Bonetti, G.; Savini, R.; Jalil, N.; Bonini, D.; Basko, C.; Galiotis, N.; *et al.* Uniaxial Strain in Graphene by Raman Spectroscopy: G Peak Splitting, Grüneisen Parameters, and Sample Orientation. *Phys. Rev. B* **2009**, *79*, 205433.

33. Ataca, C.; Ataca, M.; Topsakal, E.; Aktürk, S.; Ciraci, A. Comparative Study of Lattice Dynamics of Three- and Two-Dimensional MoS$_2$. *J. Phys. Chem. C* **2011**, *115*, 16354–16361.

34. Rice, C.; Rice, R.; Young, R.; Zan, U.; Bangert, D.; Wolverson, T.; Georgiou, R.; Jalil, K.; Novoselov Raman-Scattering Measurements and First-Principles Calculations of Strain-Induced Phonon Shifts in Monolayer MoS$_2$. *Phys. Rev. B* **2013**, *87*, 081307.

35. Jian, Y. C.; Lin, D. Y.; Wu, J. S.; Huang, Y. S. Optical and Electrical Properties of Au- and Ag-Doped ReSe$_2$. *Jpn. J. Appl. Phys.* **2013**, *52*, 04CH06.

36. Ho, C. H.; Huang, C. E. Optical Property of the near Band-Edge Transitions in Rhenium Disulfide and Diselenide. *J. Alloys Compd.* **2004**, *383*, 74–79.

37. Vanderbilt, D. Soft Self-Consistent Pseudopotentials in a Generalized Eigenvalue Formalism. *Phys. Rev. B* **1990**, *41*, 7892–7895.

38. Blöchl, P. E. Projector Augmented-Wave Method. *Phys. Rev. B* **1994**, *50*, 17953–17979.

39. El-Bana, M. S.; Wolverson, D.; Russo, S.; Balakrishnan, G.; Paul, D. M.; Bending, S. J. Superconductivity in Two-Dimensional NbSe$_2$ Field Effect Transistors. *Supercond. Sci. Technol.* **2013**, *26*, 125020.

40. Windom, B.; Windom, W. G.; Sawyer, D.; Hahn, A. Raman Spectroscopic Study of MoS$_2$ and MoO$_3$: Applications to Tribological Systems. *Tribol. Lett.* **2011**, *42*, 301–310.

41. Beattie, I. R.; Ozin, G. A. Vibrational Spectrum of Gaseous, Liquid, and Solid Re$_2$O$_7$. *J. Chem. Soc. A* **1969**, 2615–2619.

42. Purans, J.; Purans, A.; Kuzmin, E.; Cazzanelli, G.; Mariotto Disorder-Induced Raman Scattering in Rhenium Trioxide (ReO$_3$). *J. Phys.: Condens. Matter* **2007**, *19*, 226206.

43. Sugai, S. Photoinduced Tellurium Precipitation in CdTe. *Jpn. J. Appl. Phys.* **1991**, *30*, L1083.

44. Castellanos Gomez, A.; Castellanos Gomez, M.; Barkelid, A. M.; Goossens, V. E.; Calado, H. S. J.; van der Zant, G. A.; Steele Laser-Thinning of MoS$_2$: On Demand Generation of a Single-Layer Semiconductor. *Nano Lett.* **2012**, *12*, 3187–3192.

45. Mizoguchi, K.; Nakashima, S. Determination of Crystallographic Orientations in Silicon Films by Raman-Microprobe Polarization Measurements. *J. Appl. Phys.* **1989**, *65*, 2583–2590.

46. Dumcenco, D. O.; Huang, Y. S.; Liang, C. H.; Tiong, K. K. Optical Characterization of Niobium-Doped Rhenium Disulphide Single Crystals. *J. Appl. Phys.* **2007**, *102*, 083523.

47. Dumcenco, D. O.; Huang, Y. S.; Liang, C. H.; Tiong, K. K. Optical Characterization of Au-Doped Rhenium Diselenide Single Crystals. *J. Appl. Phys.* **2008**, *104*, 063501.

48. Dumcenco, D. O.; Huang, W. Y.; Huang, Y. S.; Tiong, K. K. Anisotropic Optical Characteristics of Au-Doped Rhenium Diselenide Single Crystals. *J. Alloys Compd.* **2009**, *480*, 104–106.

49. Yu, P. Y.; Cardona, M. *Fundamentals of Semiconductors: Physics and Materials Properties*, 4th ed.; Springer: Heidelberg, 2010.

50. Wang, Y. Y.; Ni, Z. H.; Shen, Z. X.; Wang, H. M.; Wu, Y. H. Interference Enhancement of Raman Signal of Graphene. *Appl. Phys. Lett.* **2008**, *92*, 043121.

51. Yoon, D.; Moon, H.; Son, Y.-W.; Choi, J. S.; Park, B. H.; Cha, Y. H.; Kim, Y. D.; Cheong, H. Interference Effect on Raman Spectrum of Graphene on SiO_2/Si. *Phys. Rev. B* **2009**, *80*, 125422.

52. Schedin, F.; Lidorikis, E.; Lombardo, A.; Kravets, V. G.; Geim, A. K.; Grigorenko, A. N.; Novoselov, K. S.; Ferrari, A. C. Surface-Enhanced Raman Spectroscopy of Graphene. *ACS Nano* **2010**, *4*, 5617–5626.

53. Li, S. L.; Miyazaki, H.; Song, H.; Kuramochi, H.; Nakaharai, S.; Tsukagoshi, K. Quantitative Raman Spectrum and Reliable Thickness Identification for Atomic Layers on Insulating Substrates. *ACS Nano* **2012**, *6*, 7381–7388.

54. Huang, T.-P.; Huang, D.-Y.; Lin, Y.-C.; Kao, J.-D.; Wu, Y.-S.; Huang Polarized Thermoreflectance and Reflectance Study of ReS_2 and ReS_2:Au Single Crystals. *Jpn. J. Appl. Phys.* **2011**, *50*, 04DH17.

55. Garcia, R.; Perez, R. Dynamic Atomic Force Microscopy Methods. *Surf. Sci. Rep.* **2002**, *47*, 197–301.

56. Nemes-Incze, P.; Osvath, Z.; Kamaras, K.; Biro, L. P. Anomalies in Thickness Measurements of Graphene and Few Layer Graphite Crystals by Tapping Mode Atomic Force Microscopy. *Carbon* **2008**, *46*, 1435–1442.

57. Clark, S. J.; Segall, M. D.; Pickard, C. J.; Hasnip, P. J.; Probert, M. I. J.; Refson, K.; Payne, M. C. First Principles Methods Using Castep. *Z. Kristallogr.* **2005**, *220*, 567.

58. Paolo, G.; Stefano, B.; Nicola, B.; Matteo, C.; Roberto, C.; Carlo, C.; Davide, C.; Guido, L. C.; Matteo, C.; Ismaila, D.; *et al.* Quantum Espresso: A Modular and Open-Source Software Project for Quantum Simulations of Materials. *J. Phys.: Condens. Matter* **2009**, *21*, 395502.

59. Monkhorst, H. J.; Pack, J. D. Special Points for Brillouin-Zone Integrations. *Phys. Rev. B* **1976**, *13*, 5188–5192.

60. Baroni, S.; de Gironcoli, A.; Dal, C. Phonons and Related Crystal Properties from Density-Functional Perturbation Theory. *Rev. Mod. Phys.* **2001**, *73*, 515–562.

61. Kokalj, A. Computer Graphics and Graphical User Interfaces as Tools in Simulations of Matter at the Atomic Scale. *Comput. Mater. Sci.* **2003**, *28*, 155–168.